



# Cyclic voltammetry with non-triangular waveforms: Electrochemically reversible systems



Yuki Uchida<sup>1</sup>, Enno Kätelhön<sup>1</sup>, Richard G. Compton<sup>\*</sup>

Department of Chemistry, Physical and Theoretical Chemistry Laboratory, Oxford University, South Parks Road, Oxford OX1 3QZ, United Kingdom

## ARTICLE INFO

### Keywords:

Cyclic voltammetry  
Non-triangular waveforms  
Finite difference simulation  
Fractional calculus

## ABSTRACT

Cyclic voltammetry is typically performed using triangular waveforms, however, complications inevitably arise from the discontinuous nature of the differentiated triangular wave: As the capacitive current contributions are proportional to the derivative of the applied electrode potential, the measured current is (at least theoretically) discontinuous, which experimentally manifests in perturbed voltammetric data following minima and maxima in the applied triangular wave that is mostly due to unavoidable parasitic capacitances. We herein investigate voltammetry using alternative waveforms which on the one hand circumvent such difficulties and on the other exhibit unique features in the voltammetric response. We show that these features immediately reveal the formal potential of an investigated reaction that is readily available without any need for further data processing, and enable a new and easy-to-use route to determine formal potentials.

## 1. Introduction

For decades cyclic voltammetry [1–4] has been the key technique in electrochemistry and still today remains an integral part of most electrochemical and electro-analytical studies published. In a typical cyclic voltammetry experiment, an electrode is set in contact with an electrolyte solution containing an analyte of interest. The surface is then biased with respect to the solution, while a triangular potential wave  $E(t)$  is applied to the electrode relative to a reference electrode:

$$E(t) = \begin{cases} \pm \sigma t + E(t=0) & \text{for } t < t_{1/2} \\ \mp \sigma(t - t_{1/2}) + E(t=t_{1/2}) & \text{for } t \geq t_{1/2} \end{cases} \quad (1)$$

where  $\sigma$  is the scan rate and  $t_{1/2}$  is half of the duration of one cycle. During the potential scan, the electrode current, the current through the solid–liquid interface, is monitored and enables diverse insights into the nature of the reaction at the electrode surface. As a vast amount of accessible and easy-to-use theory exists [5], numerous physical quantities can be readily extracted from voltammetric data including analyte concentrations, diffusion constants, and rate constants to just name a few.

Aside from the great opportunities offered by cyclic voltammetry using the triangular wave (Eq. (1)), experimental challenges inevitably result from the discontinuity of the potential's first derivative with respect to time. As capacitive contributions  $I_c$  to the measured current ( $I = I_c + I_p$ ) are proportional to the first derivative of the applied

electrode potential  $E(t)$  with respect to time:

$$I_c \propto d_t E(t). \quad (2)$$

$I_c$  is discontinuous, which entails perturbed voltammetric data following turning points at  $t = n \cdot t_{1/2}$ ,  $n \in \mathbb{N}^0$ . The perturbations are mostly due to parasitic capacitances present in the measurement set-up, which may in a complex fashion depend on parameters such as the scan rate, potential, and current magnitude, and hence can typically not be distinguished from actual voltammetric data. A more detailed discussion on capacitive effects can be found in recent literature [6]. While such perturbations are of course present at any time of the experiment and generally affect all data, their influence may however be much larger at discontinuities in the current where they pose a much greater challenge to the acquisition and quantitative analysis of experimental results and which should therefore desirably be avoided.

In this work, we present an alternative approach to cyclic voltammetry using a slightly different waveform to the above triangular wave to prevent discontinuities in the measured electrode current. Related voltammetry is investigated in much detail and an expression for the height of the first peak is established akin to the well-known Randles–Ševčík equation [7,8]. Our analysis further reveals that the proposed method gives rise to unique voltammetric features that can be exploited to determine the formal potential of a reaction at an ease and clarity far beyond means offered by triangular wave cyclic voltammetry.

<sup>\*</sup> Corresponding author at: Physical and Theoretical Chemistry Laboratory, South Parks Road, Oxford OX1 3QZ, England, United Kingdom.

E-mail address: [richard.compton@chem.ox.ac.uk](mailto:richard.compton@chem.ox.ac.uk) (R.G. Compton).

<sup>1</sup> The two authors contributed equally to this work.

## 2. Theory

In the following section, the proposed method of an alternative non-triangular waveform is explained and a theoretical model introduced. We further introduce practical dimensionless coordinates and two different computational approaches, finite difference simulation and computation based on fractional calculus, which complement each other.

### 2.1. Theoretical model

We investigate a simple one-electron electrochemically-reversible reduction reaction of A to B at a planar macroelectrode under diffusion-only conditions, where both species have equal diffusion coefficients:



The system is assumed to be fully-reversible in which the electrode kinetics are much faster in comparison to the mass transport resulting in a Nernstian equilibrium at the electrode surface: [2,9,10]

$$E = E_f^0 + \frac{RT}{F} \ln \frac{c_A(x=0)}{c_B(x=0)} \quad (4)$$

where  $E$  is again the applied potential,  $E_f^0$  is the formal potential of the A/B couple, and  $c_A(x=0)$  and  $c_B(x=0)$  are the surface concentrations of species A and B, respectively. In this system, only diffusion is considered as means of mass transport of the analytes to the electrode surface with no convection and the presence of a sufficiently high concentration of supporting electrolyte is assumed so that migration can be neglected [11–14]. It is, however, important to note that with sufficiently long scan duration times, convection may affect experimental results [2,3,15–17]. The transport of analytes is hence described via the one-dimensional diffusion equation given by Fick's second law, which relates the change in concentration,  $c$ , over space,  $x$ , with time,  $t$ : [18,19]

$$\frac{\partial c_j}{\partial t} = D_j \frac{\partial^2 c_j}{\partial x^2} \quad (5)$$

where  $j$  is the species of interest and  $D$  is the diffusion coefficient of the said species. In order to solve the diffusion equation, boundary conditions are established for the case where only species A is present in the bulk solution [2,18], and the concentration of both A and B is uniform in space:

$$t \leq 0, \text{ all } x, \quad c_A = c_A^*, \quad c_B = 0. \quad (6)$$

As  $t$  increases, both  $c_A$  and  $c_B$  change, however, at a distant significantly far from the electrode, no reaction is observed and the solution remains the same as the initial condition:

$$t > 0, \quad x \rightarrow \infty, \quad c_A = c_A^*, \quad c_B = 0. \quad (7)$$

Since both species have the same diffusion coefficient and by conservation of mass, the amount of A consumed at the electrode equals the amount of B gained:

$$t > 0, \quad x = 0, \quad -\frac{\partial c_A}{\partial x} = \frac{\partial c_B}{\partial x} \quad (8)$$

and, due to the symmetry of all boundary conditions with respect to the exchange of A and B, the following condition holds at any point in space:

$$c_A(x, t) + c_B(x, t) - c_A^* = 0. \quad (9)$$

### 2.2. Proposed method

In contrast to a triangular wave, the here-introduced method uses a cosine potential wave with varying powers, while the scanned potential window is shifted between different experiments. The cosine potential

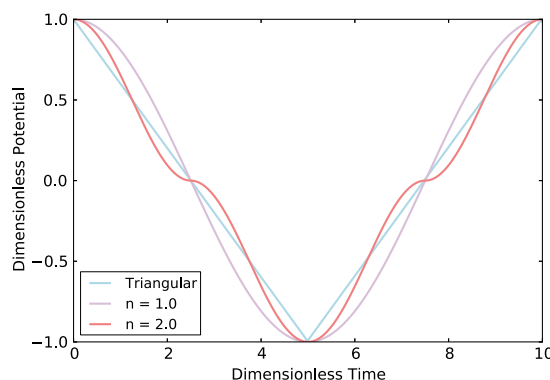


Fig. 1. Triangular, cosine, and cosine square potential waves centred at 0 with an amplitude of 1.

wave equation is given as:

$$E(i) = A \cdot |\cos(2\pi \cdot a \cdot i \Delta t)|^n \cdot \frac{\cos(2\pi \cdot a \cdot i \Delta t)}{|\cos(2\pi \cdot a \cdot i \Delta t)|} + E_{shift} \quad (10)$$

where  $A$  is the amplitude of the wave in volts,  $a$  is an auxiliary coefficient defined as  $\frac{\epsilon^2}{D} \cdot \frac{F}{RT} \cdot \nu_{avg} \cdot \frac{1}{4A}$  in which  $\epsilon$  is the radius of the electrode,  $D$  is the diffusion coefficient of the species of interest,  $F$  is the Faraday constant,  $R$  is the gas constant,  $T$  is the temperature, and  $\nu_{avg}$  is the average scan rate measured in volts per second. The other parameters,  $i$ , is the time step,  $\Delta t$  is the difference between each time step,  $n$  is the power of the function, and  $E_{shift}$  is the offset of the wave. It is herein noted that although sine waves and cosine waves are used in AC voltammetry, this paper focuses on the use of cosine waves in cyclic voltammetry.

As can be seen in Fig. 1, the duration time is kept the same between the triangular and non-triangular potential waves but the instantaneous scan rate at any potential differs depending on the applied potential for non-triangular waveforms. In addition, the figure reveals that there are no discontinuities in the first temporal derivative of the potential and the above-bespoken perturbations arising from parasitic capacitances will not be observed in experimental data. We further note that a plateau is observed for the cosine square wave at the midpoint of the applied potential range, which moves up or down depending on the potential window shift,  $E_{shift}$ .

### 2.3. Dimensionless coordinates

For simplicity and both easier and general application of our results to various experimental conditions, dimensionless parameters [18] are used in the following manuscript, while conversion factors are shown in Table 1. Given these expressions, the cosine equation can now be expressed in terms of dimensionless parameters where  $A$  is the amplitude

Table 1  
Dimensionless parameters [18].

Parameter	Normalization
Concentration	$C_j = \frac{c_j}{c_A^*}$
Diffusion coefficient	$d_j = \frac{D_j}{D_A}$
Spatial coordinate	$X = \frac{x}{\epsilon}$
Time	$\tau = \frac{D_A t}{\epsilon^2}$
Potential	$\theta = \left(\frac{F}{RT}\right)(E - E_f^0)$
Scan rate	$\sigma = \left(\frac{\epsilon^2}{D_A}\right)\left(\frac{F}{RT}\right)\nu$
Current	$J = \frac{I}{\pi \epsilon F D_A c_A^*}$

of the dimensionless potential,  $a = \frac{\sigma_{avg}}{4A}$ , and  $E_{shift} = E_{avg} - E_f^0$  for which  $E_f^0$  is set to equal 0. The diffusion equation also transforms to:

$$\frac{\partial C_j}{\partial \tau} = d_j \frac{\partial^2 C_j}{\partial X^2} \quad (11)$$

where  $d_j = 1$ .

Simulations were run using several scan rates ranging from  $\sigma = 10^2$  to  $10^7$  while the results shown below were obtained for  $\sigma = 10^4$  unless stated otherwise. Other parameters used for simulations are:  $\Delta\theta = 0.0001$ ,  $\omega = 1.05$ , and  $h = 10^7$ .

#### 2.4. Simulation via finite differences

We simulate the above theoretical model via a finite differences approach. To this end, the dimensionless Fick's second law (Eq. (11)) is discretized using the backward implicit method explained in detail in the Supporting Information.

The numerical procedure was implemented in C++ and data processing and visualisation was done in Python via the software packages NumPy and matplotlib. We appreciate that comprehensive software testing [20] is a crucial requirement for the development of electrochemical simulation software and have therefore carried out various tests on our code: Peak-to-peak separations and peak heights were compared with theoretical predictions and convergence tests were run.

#### 2.5. Simulation via fractional calculus

In addition to the finite differences approach outlined in the previous section, we complement our findings through the application of fractional calculus in electrochemistry as pioneered by Oldham. Considering the above theoretical model, our approach follows the method described by Oldham [21], which is summarized below. Mass transport Eq. (5) can be represented in Laplace space:

$$s\bar{c}_i(x, s) - c_i^* = D \frac{d^2}{dx^2} \bar{c}_i(x, s) \quad (12)$$

where  $\bar{c}_i(x, s)$  is the Laplace transform of  $c_i(x, t)$ , and  $s$  is the complex frequency parameter. Given the structure of the so-obtained partial differential equation, it is evident that concentration profiles of the form:

$$\bar{c}_i(x, t) = \frac{c_i^*}{s} + \Gamma(s) \exp\left(-x \sqrt{\frac{s}{D}}\right) \quad (13)$$

provide valid solutions where  $\Gamma(s)$  is an arbitrary function of  $s$ . We next eliminate  $\Gamma(s)$  by considering Fick's first law in Laplace space:

$$\bar{j}_i(x, s) = -D \frac{d}{dx} \bar{c}_i(x, s) \quad (14)$$

where evaluation of Eq. (13) in terms of Eq. (14) and comparison with Eq. (13) yields an expression for  $\bar{c}_i$  that is independent of  $\Gamma(s)$ :

$$\bar{c}_i(x, s) = \frac{c_i^*}{s} + \frac{1}{\sqrt{Ds}} \bar{j}_i(x, s). \quad (15)$$

Convolution theorem enables the back-transformation of the concentration profiles from the Laplace into the time-domain, where the evaluation of the flux at the electrode surface  $x = 0$  provides us with a general solution of the concentration profile:

$$c_i(x = 0, t) = c_i^* + \frac{1}{\sqrt{D}} \frac{d^{-1/2}}{dt^{-1/2}} j_i(x = 0, t). \quad (16)$$

Considering the conservation of charge at the interface,  $j_A(x = 0, t) = -j_B(x = 0, t)$  and Faraday's law  $I_i = FAj_i$ , enable us to link the equations for species A and B in the following expression [22]:

$$-(c_A^* - c_A(x = 0, t)) = \frac{1}{FA\sqrt{D}} \frac{d^{-1/2}}{dt^{-1/2}} I(t) = (c_B^* - c_B(x = 0, t)). \quad (17)$$

Aside from the conservation of mass,  $j_A + j_B = 0$  at the electrode surface, no further physical aspects of the reactions kinetics have so far been considered in the derivation of Eq. (17) and the result is independent of the electrode kinetics. In order to implement the Nernstian reaction considered in the context of this study, we re-write [22] Nernst equation in terms of the bulk concentrations  $c_A^*$  and  $c_B^*$ :

$$\exp\left(\frac{F}{RT}(E(t) - E(t=0))\right) = \frac{c_A(x=0, t)}{c_B(x=0, t)} \cdot \frac{c_B^*}{c_A^*} \quad (18)$$

where we imply that system is in equilibrium at the initially applied potential  $E(t = 0)$ , i.e.  $E(t = 0) = RT/F \cdot (\ln(c_A^*) - \ln(c_B^*))$ . The combination of the Eqs. (17) and (18), and straight forward algebra yield an expression [22] for the voltammetric current response as a function of the applied potential wave and features the form:

$$I(t) = \frac{d^{+1/2}}{dt^{+1/2}} f(E(t)) \quad (19)$$

with:

$$f(E(t)) = FAc_B^* \sqrt{D} \left( 1 - \frac{1 + \frac{c_B^*}{c_A^*}}{\exp\left(\frac{F}{RT}(E(t) - E(t=0))\right) + \frac{c_B^*}{c_A^*}} \right) \quad (20)$$

In combination with a suitable algorithm to carry out the semi-integration, this expression can be used to evaluate the voltammetric response to an arbitrary potential profile  $E(t)$ . In this work, we continue to follow the approach discussed by Oldham [22] and approximate the semi-derivative numerically as:

$$\frac{d^{+1/2}}{dx^{+1/2}} f(t) = \frac{1}{\sqrt{\delta}} \sum_{j=0}^{(t/\delta)-1} w_j f(t - j\delta) \quad (21)$$

with:

$$w_j = \left(1 - \frac{3}{2j}\right) w_{j-1} \quad \text{and} \quad w_0 = 1. \quad (22)$$

For the purpose of this study, the above numerical model was implemented in C++, which enables the calculation of a large number of voltammograms on a timescale far superior to typical finite difference or finite element simulations. Similar to the finite difference simulations discussed above, extensive software testing [20] was carried out: Peak-to-peak separations and peak heights were compared with theoretical predictions, and convergence tests were conducted.

### 3. Results and discussion

The following section discusses the opportunities arising from the proposed voltammetric method. To this end, we first focus on the implications of the altered voltammetric wave on the capacitive current before we address the voltammetric response to the above cosine wave with an exponent of one. Finally, the study is concerned with the voltammetry observed for greater exponents and outlines an entirely novel but highly practical approach to the determination of the formal potential of a redox couple.

#### 3.1. Capacitive currents

Whenever a potential is applied to an electrode in an experimental system, a double layer forms at the interface between the electrode and the electrolyte solution as electrostatic effects compensate for the charge difference and effectively screen the electrode potential in solution [3,23]. The double layer acts as a capacitor and thereby generates a capacitive current contribution to electrode current if the

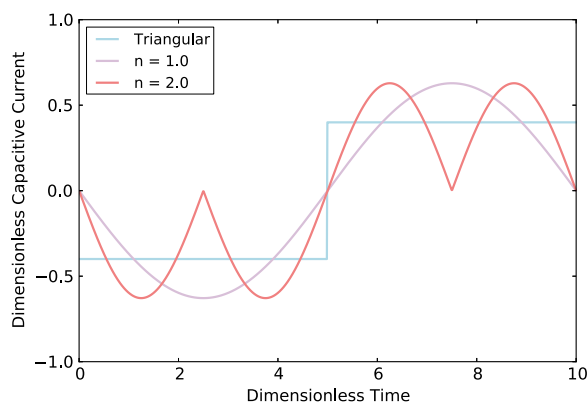


Fig. 2. Capacitive current of triangular, cosine, and cosine square potential waves centred at 0. The double-layer capacitance is assumed to be potential independent.

electrode potential is varied: see Eq. (2). Fig. 2 shows the capacitive currents for triangular, cosine, and cosine square potential waves obtained by taking the derivative of each pulse wave in Fig. 1, where the latter two are calculated via Eq. (10) and  $n$  is set to one and two, respectively.

For the linear sweep, a discontinuous capacitive current is observed at the point where the potential sweep is reversed, which is intuitive from Fig. 1 since the slope changes sign in equal magnitude at said point. In reality a distinct step is not seen because of the time constant of the electrochemical cell, however, as discussed in the previous section, the discontinuity in the capacitive current disrupts the voltammogram obtained in experiments and often results in an unwanted complication of the measured data. In contrast, cosine and cosine square waves are both continuous at the point of reversal as well as at all other points throughout the entire sweep, minimising the effect of capacitive current drop and the perturbation of the voltammogram.

Fig. 3 shows the theoretical behavior of voltammograms when a capacitive current is considered in the modelling of triangular, cosine, and cosine square potential waves. The arrows indicate the direction of the sweep. As expected, the voltammogram with triangular waveform shows a step caused by the capacitive current at the point of reversal whereas voltammograms with cosine and cosine square waves show minimal perturbation at the said point. The capacitive current was calculated using the following equation:

$$I_k = K\nu A_{ele} \quad (23)$$

where  $I_k$  is the capacitive current,  $K$  is the capacitance per surface area,  $\nu$  is the scan rate, and  $A_{ele}$  is the area of the electrode. This equation was transformed into dimensionless coordinates using the conversion factors listed in Table 1 in order to obtain a dimensionless expression for the capacitance,  $K'$ :

$$K' = \frac{KRT}{\epsilon F^2 c_A^*} \quad (24)$$

Here,  $K = 20 \mu\text{F}/\text{cm}^2$ ,  $\epsilon = 10^{-3} \text{ m}$ , and  $c_A^* = 1.0 \text{ mol}/\text{m}^3$ .

### 3.2. Voltammetry obtained using a cosine potential wave when $n = 1$

Fig. 4 shows a voltammogram simulated for a cosine pulse wave that is symmetric with respect to the reaction's formal potential using a scan rate of  $\sigma = 10^4$ . The red dotted line herein corresponds to the peak current value obtained from the Randles-Ševčík equation which in dimensional form is: [18,24,25]

$$I_p = -0.446FAc_A^* \sqrt{\frac{FD_A\nu}{RT}} \quad (25)$$

which shows a square root dependence on the scan rate,  $\nu$  [26,27]. Using the aforementioned conversion factors between dimensional and

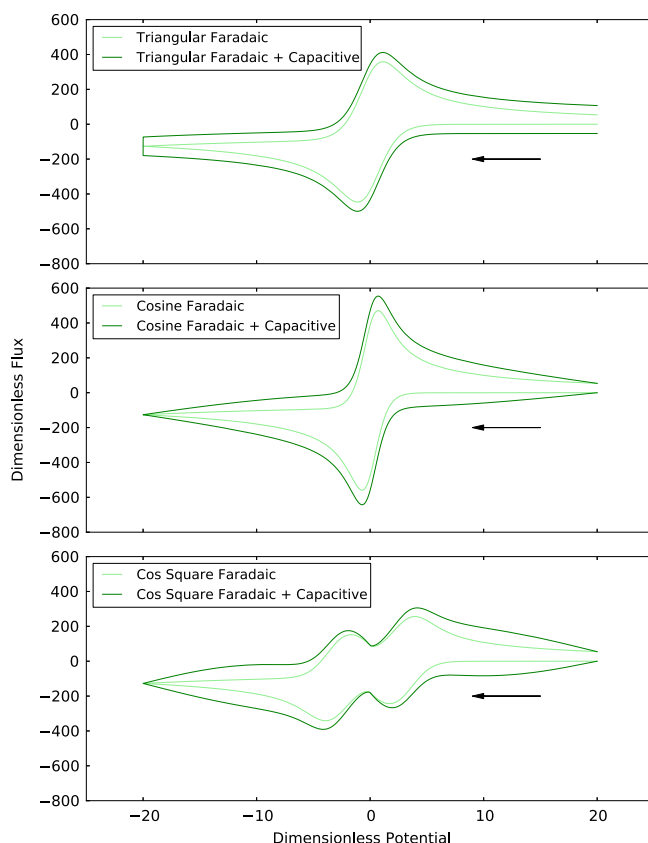


Fig. 3. A comparison between voltammograms with and without capacitive perturbations run at a scan rate of  $\sigma = 10^6$  and with a smaller window.

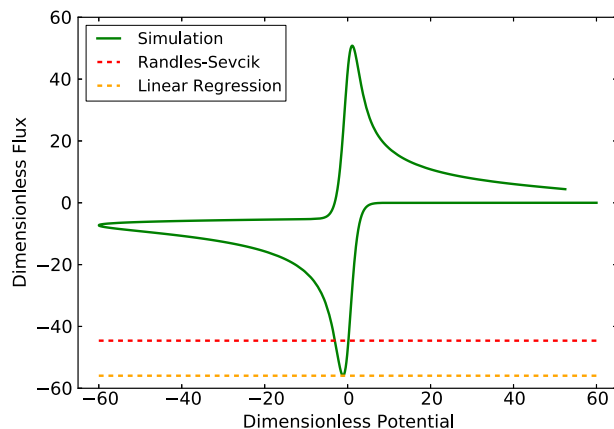


Fig. 4. Voltammogram using cosine potential wave centered at 0. (For interpretation of the references to color in this figure, the reader is referred to the web version of this article.)

dimensionless coordinates, Eq. (25) was converted into its dimensionless form:

$$J_p = -0.446\sqrt{\sigma}. \quad (26)$$

The value indicated by the horizontal yellow line is the peak current observed in the simulated voltammogram. In the figure, it can be clearly seen that the simulated peak current exceeds the peak current arising from a standard triangular wave as described by the Randles-Ševčík equation. This can be understood by comparing the sweep rates in the region of the formal potential; although the durations of both, the triangular and the cosine wave measured over the full voltammetric sweep are equal, their scan rates in the region of the formal potential

differ with the cosine wave featuring a higher transient scan rate. The observed current response is hence elevated as higher scan rates lead to increased rates of material reacting.

The peak currents of the cosine model are further investigated in analogy with the Randles-Ševčík equation by fitting a linear function to the graph obtained from plotting the peak currents versus the square root of the scan rate as shown in Fig. 5.

In the figure, blue and yellow dots correspond to the peak heights of voltammograms simulated with triangular and cosine waves, respectively, at each dimensionless scan rate between  $10^2$  to  $10^7$ . The peak current for a triangular potential wave under one-dimensional diffusion is calculated by the Randles-Ševčík equation and is used to generate the pink line. The line passes through the centres of the dots demonstrating that the simulated results coincide with the theoretical value calculated by Eq. (26). The orange line is generated by performing a linear regression on the yellow dots, whose slope is then used to determine the coefficient of the equation for the cosine potential wave akin to the Randles-Ševčík expression:

$$J_p = -0.559\sqrt{\sigma}. \quad (27)$$

Similar to the triangular potential wave voltammogram, the peak current of the cosine potential wave voltammogram shows a square root dependence on the scan rate. The simulations were run using dimensionless parameters and hence the mathematical expression for the linear regression shown in Fig. 5 is obtained in dimensionless coordinates. This can then be converted to a dimensional expression using the conversion factors listed in Table 1 and becomes:

$$I_p = -0.559FAc_A^* \sqrt{\frac{FD_A\nu}{RT}}. \quad (28)$$

Eq. (28) shows approximately a 25% increase in the peak current compared to that obtained from the Randles-Ševčík equation. The reasoning behind this can again be attributed to the steeper slope of the applied potential waveform around the formal potential where the electron transfer occurs most significantly.

### 3.3. Voltammetric effects of cosine square potential wave when $n > 1$

When the value of  $n$  in Eq. (10) is larger than 1, a plateau is found in the applied potential as shown in Fig. 1, which becomes more pronounced with increasing  $n$ . The plateau, which signifies a temporary halt in the potential sweep, results in a double peak in the voltammogram that is most apparent for potential waves that are approximately symmetric with respect to the formal potential but diminishes at other potential shifts.

Fig. 6 shows a close-up of the voltammograms obtained using a cosine square pulse wave with different potential shifts in dimensionless coordinates (A full representation of the voltammogram is presented in the Supporting Information) from right to left and back to right as the arrow indicates. At  $E_{avg} - E_f^0 = 0^2$  and in its vicinity, two distinct peak heights are observed. However, Fig. 6 shows that when the potential shift is significantly negative, only one peak is observed whereas when the potential shift is significantly positive, one of the peaks disappears. This behavior is clearer when the peak height is plotted against the potential shift.

Fig. 7 shows the dimensionless peak heights of the voltammograms obtained for the cosine pulse wave ( $n = 1$ ) and the cosine square pulse wave ( $n = 2$ ) against the dimensionless potential shift. The cosine peak heights represented by yellow dots shows only a little variation as the potential is shifted whereas the cosine square peak heights exhibit two

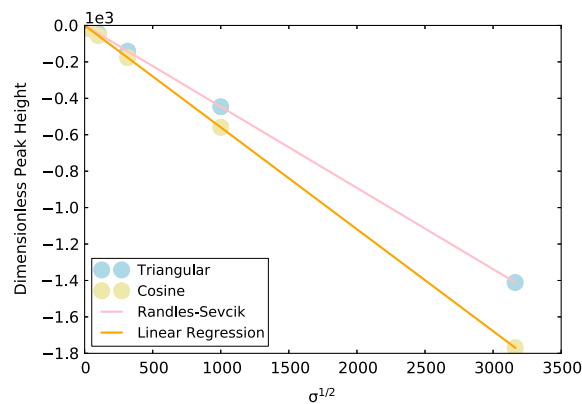


Fig. 5. Linear regression of peak heights for triangular and cosine potential waves. (For interpretation of the references to color in this figure, the reader is referred to the web version of this article.)

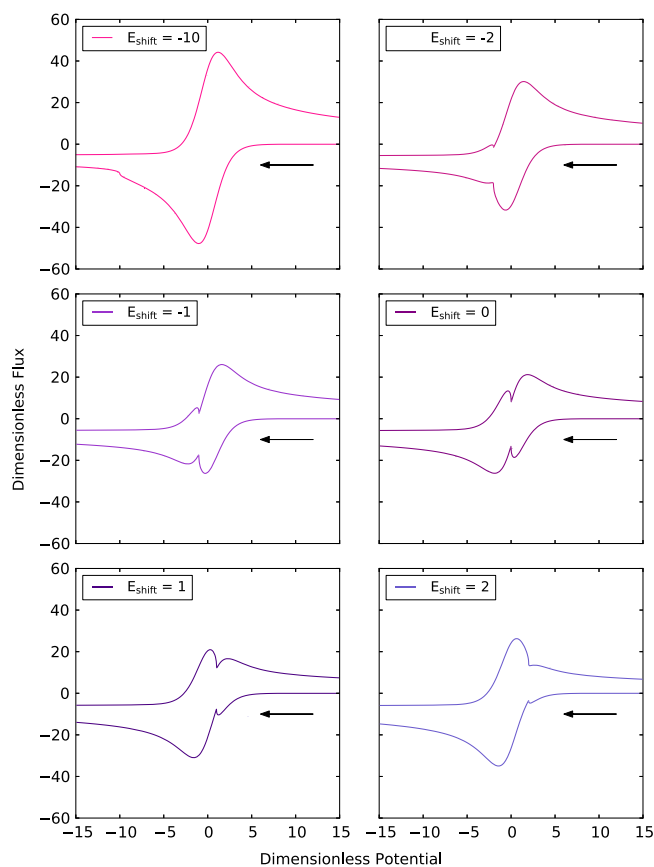


Fig. 6. Close-up of cosine graphs for  $n = 2$  with different potential shifts with respect to the formal potential. The top left voltammogram corresponds to when the potential wave is shifted  $-10$  dimensionless potential units, the top right voltammogram corresponds to when the potential wave is shifted  $-2$  units, the middle left corresponds to when the potential wave is shifted  $-1$  units, the middle right is when the potential wave is symmetric, the bottom left corresponds to when the wave is shifted  $1$  units, and the bottom right corresponds to when the wave is shifted  $2$  units.

peaks emerging when the potential shift is around  $-2$  dimensionless potential units. The light purple dots and the solid orange line herein represent the first peak and the dark purple dots and the dashed orange line represent the second. As discussed above, the absolute height of the first peak decreases and approaches 0 as the potential shift becomes increasingly positive while both peaks merge as the shift becomes smaller. A sudden change in the peak height of the second peak is observed around the potential shift of  $-2$  dimensionless potential units,

$$E_{avg} = \frac{1}{t_{max}} \int_0^{t_{max}} E(t) dt \quad (29)$$

where  $t_{max}$  is the maximum value of the duration time for the scan.



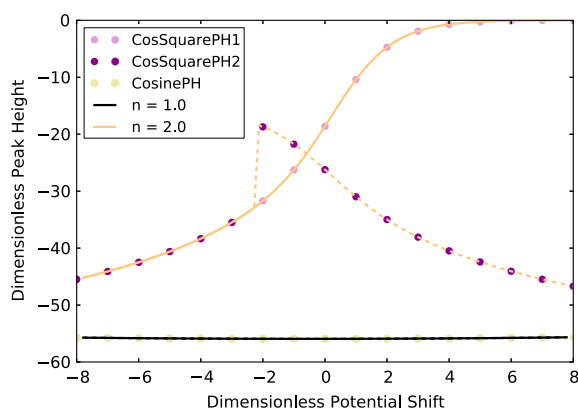


Fig. 7. Changes in cosine square peak heights with the potential shift with respect to the formal potential. (For interpretation of the references to color in this figure, the reader is referred to the web version of this article.)

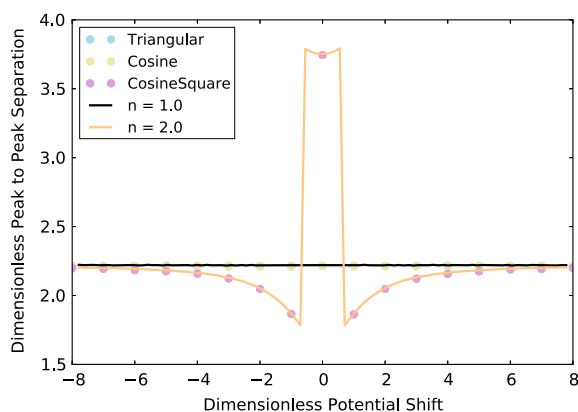


Fig. 8. Changes in peak to peak separation with different potential shift.

which is the threshold above which two peaks are seen. Below  $-2$  only one peak is visible, but at approximately the said potential shift, the second peak additionally emerges and peak one diminishes as evident from Fig. 6. Beyond the point of intersection of the dark purple and light purple dots, the two peaks swap heights and the second peak becomes dominant while the first gradually diminishes. In the figure, the dots signify results obtained from the finite difference method, whereas the solid and dashed lines correspond to the results from fractional calculus, and as can be seen, the two results agree with each other.

The double peak caused by the cosine square wave results in a peak-to-peak separation as shown in Fig. 8.

Fig. 8 shows the changes in peak-to-peak separation of the voltammograms simulated using the potential waves given in Fig. 1 with varying potential shifts. For the cosine wave when  $n = 1$ , the peak-to-peak separation potential remains approximately 2.2 in dimensionless units, which in dimensional term corresponds to 57 mV (the standard peak-to-peak separation of a reversible system at 298 K [2,27–31]), and is also evident from the nearly perfect overlap with the results from the triangular waveform. On the other hand, the peak-to-peak separation changes markedly depending on the potential shift when  $n > 1$ . As the potential shift approaches 0, the peak-to-peak separation decreases but at  $E_{avg} - E_f^0 = 0$  and in its immediate vicinity, the peak-to-peak separation shows a sharp increase. Here, the dots, again, represent the results obtained from the finite difference method and the solid lines represent the results from fractional calculus. The fact that double peaks appear and drastic changes in peak-to-peak separation are observed with varying potential shifts suggest that cosine waves with  $n > 1$  can be used to determine the formal potential of a species.

In practice, this would be performed by applying the cosine wave

given by Eq. (10) to an electrode and measuring the peak-to-peak separation of the voltammogram obtained. The same process would be repeated with different  $E_{shift}$  values until a sharp increase in the peak-to-peak separation is observed. The cosine potential wave may also be beneficial in ultrafast voltammetry to change some common complications [32,33] that have been addressed in previous literature.

#### 4. Conclusions

We propose a novel approach to cyclic voltammetry, where a non-triangular waveform is repeatedly applied while the wave's average potential,  $E_{avg}$ , is shifted with respect to the reference potential. By this means, two challenges can be addressed; first, in triangular wave cyclic voltammetry, an instantaneous change in capacitive current is observed at the point of reversal where it causes a perturbation of the voltammogram. In contrast, the here-proposed waveform features a continuous slope across the entire potential range, minimizing the disruption of the Faradaic current at the said point. Secondly, the proposed wave form yields double peaks in the voltammogram, which separately vary in intensity depending on the difference between  $E_{avg}$  and  $E_f^0$ , and result in a sharp increase in the peak-to-peak separation at  $E_{avg} - E_f^0 = 0$ . This effect can be exploited as a tool to experimentally determine the formal potential of a reaction.

#### Acknowledgments

The research leading to these results has received partial funding from the European Research Council under the European Union's Seventh Framework Programme (FP/2007-2013)/ERC Grant Agreement no. [320403].

#### Appendix A. Supplementary data

Supplementary data to this article can be found online at <http://dx.doi.org/10.1016/j.jelechem.2017.08.008>.

#### References

- [1] R.S. Nicholson, I. Shain, Theory of stationary electrode polarography. Single scan and cyclic methods applied to reversible, irreversible, and kinetic systems. *Anal. Chem.* 36 (4) (1964) 706–723.
- [2] R.G. Compton, C.E. Banks, *Understanding Voltammetry*, Imperial College Press, 2010.
- [3] A.J. Bard, L.R. Faulkner, *Electrochemical Methods: Fundamentals and Applications*, John Wiley & Sons Inc., 2000.
- [4] C. Batchelor-McAuley, E. Kätelhön, E.O. Barnes, R.G. Compton, E. Laborda, A. Molina, Recent advances in voltammetry, *ChemistryOpen* 4 (3) (2015) 224–260.
- [5] E. Kätelhön, Theory in modern electrochemistry: science for the academic ivory tower or a vital tool for today's research? *Res. Rev. Electrochem.* 8 (1) (2017) E1–E2.
- [6] K. Cinková, M. Clark, S.V. Sokolov, C. Batchelor-McAuley, L. Švorc, R.G. Compton, Improving limits of detection. Microdisc versus microcylinder electrodes, *electroanalysis* 29 (4) (2017) 1006–1013.
- [7] J.E.B. Randles, A cathode ray polarograph. Part II. — the current–voltage curves, *Trans. Faraday Soc.* 44 (1948) 327–338.
- [8] A. Ševčík, Oscillographic polarography with periodical triangular voltage, *Collect. Czech. Chem. Commun.* 13 (1948) 349–377.
- [9] J.C. Helfrick, L.A. Bottomley, Cyclic square wave voltammetry of single and consecutive reversible electron transfer reactions, *Analyt. Chem.* 81 (21) (2009) 9041–9047.
- [10] K.B. Oldham, D.J. Gavaghan, A.M. Bond, A full analytic treatment of reversible linear-scan voltammetry with square-wave modulation, *J. Phys. Chem. B* 106 (1) (2002) 152–157.
- [11] J.R. Selman, J. Newman, Free-convection mass transfer with a supporting electrolyte, *J. Electrochem. Soc.* 118 (7) (1971) 1070.
- [12] C. Amatore, A. Oleinick, I. Svir, Theoretical analysis of microscopic ohmic drop effects on steady-state and transient voltammetry at the disk microelectrode: a quasi-conformal mapping modeling and simulation, *Anal. Chem.* 80 (21) (2008) 7947–7956.
- [13] M. Ciszowska, L. Zeng, E.O. Stejskal, J.G. Osteryoung, Transport of thallium(I) counterion in polyelectrolyte solution determined by voltammetry with micro-electrodes and by pulsed-field-gradient, spin-echo NMR, *J. Phys. Chem.* 99 (30) (1995) 11764–11769.
- [14] S. Ching, R. Dudek, E. Tabet, Cyclic voltammetry with ultramicroelectrodes, *J.*

- Chem. Educ. 71 (7) (1994) 602.
- [15] C. Amatore, C. Pebay, L.A. Wang, J.-S. Warkocz, Difference between ultra-microelectrodes and microelectrodes: influence of natural convection, *Anal. Chem.* 82 (16) (2010) 6933–6939.
- [16] C.N. Reilley, G.W. Everett, R. Johns, Voltammetry at constant current: experimental evaluation, *Anal. Chem.* 27 (4) (1955) 483–491.
- [17] K. Ngamchuea, S. Eloul, K. Tschulik, R.G. Compton, Advancing from rules of thumb: quantifying the effects of small density changes in mass transport to electrodes. Understanding natural convection, *Anal. Chem.* 87 (14) (2015) 7226–7234 PMID: 26067985.
- [18] R.G. Compton, E. Laborda, K.R. Ward, *Understanding Voltammetry: Simulation of Electrode Processes*, Imperial College Press, 2013.
- [19] J. Crank, *The Mathematics of Diffusion*, Oxford University Press, 1979.
- [20] E. Kätelhön, R.G. Compton, Testing and validating electroanalytical simulations, *Analyst* 140 (8) (2015) 2592–2598.
- [21] K.B. Oldham, J.C. Myland, Modelling cyclic voltammetry without digital simulation, *Electrochim. Acta* 56 (28) (2011) 10612–10625.
- [22] K.B. Oldham, Multi-scan reversible cyclic voltammetry: is the ultimate condition approached and, if so, how fast? *J. Solid State Electrochem.* 17 (2013) 2757–2769.
- [23] H. Wang, L. Pilon, Physical interpretation of cyclic voltammetry for measuring electric double layer capacitances, *Electrochim. Acta* 64 (2012) 130–139.
- [24] I. Streeter, R. Baron, R.G. Compton, Voltammetry at nanoparticle and micro-particle modified electrodes: theory and experiment, *J. Phys. Chem. C* 111 (45) (2007) 17008–17014.
- [25] M.J.A. Shiddiky, A.A.J. Torriero, J.M. Reyna-Gonzalez, A.M. Bond, Nonadditivity of Faradaic currents and modification of double layer capacitance in the voltammetry of mixtures of ferrocene and ferrocenium salts in ionic liquids, *Analy. Chem.* 82 (5) (2010) 1680–1691.
- [26] P., R. Kant, Theory for anomalous response in cyclic staircase voltammetry: electrode roughness and unequal diffusivities, *J. Phys. Chem. C* 118 (46) (2014) 26599–26612.
- [27] E.J.F. Dickinson, J.G. Limon-Petersen, N.V. Rees, R.G. Compton, How much supporting electrolyte is required to make a cyclic voltammetry experiment quantitatively “diffusional”? A theoretical and experimental investigation, *J. Phys. Chem. C* 113 (25) (2009) 11157–11171.
- [28] Z. Ban, E. Kätelhön, R.G. Compton, Voltammetry of porous layers: staircase vs analog voltammetry, *J. Electroanal. Chem.* 776 (2016) 25–33.
- [29] G.A. Mabbott, An introduction to cyclic voltammetry, *J. Chem. Educ.* 60 (9) (1983) 697.
- [30] D.H. Evans, K.M. O’Connell, R.A. Petersen, M.J. Kelly, Cyclic voltammetry, *J. Chem. Educ.* 60 (4) (1983) 290.
- [31] A. Molina, J. Gonzalez, M.C. Henstridge, R.G. Compton, Voltammetry of electrochemically reversible systems at electrodes of any geometry: a general, explicit analytical characterization, *J. Phys. Chem. C* 115 (10) (2011) 4054–4062.
- [32] C. Amatore, C. Lefrou, New concept for a potentiostat for on-line ohmic drop compensation in cyclic voltammetry above  $300 \text{ kV s}^{-1}$ , *J. Electroanal. Chem.* 324 (1) (1992) 33–58. An international journal devoted to all aspects of electrode kinetics, interfacial structure, properties of electrolytes, colloid and biological electrochemistry.
- [33] X.-S. Zhou, B.-W. Mao, C. Amatore, R.G. Compton, J.-L. Marignier, M. Mostafavi, J.-F. Nierengarten, E. Maisonhaute, Transient electrochemistry: beyond simply temporal resolution, *Chem. Commun.* 52 (2016) 251–263.